

Quantum coherent control of non-linear thermoelectric transport in a triple-dot Aharonov-Bohm heat engine

Jayasmita Behera,¹ Salil Bedkihal,² Bijay Kumar Agarwalla,³ Malay Bandyopadhyay¹

¹*School of Basic Sciences, Indian Institute of Technology Bhubaneswar, Odisha, India 752050,*

²*A.S.E Analytics India and 110 Rue St Francois N J1E 3H6, Sherbrooke, QC, Canada,*

³*Department of Physics, Indian Institute of Science Education and Research, Pune 411008, India.*

(Dated: March 17, 2023)

We investigate the role of quantum coherence and higher harmonics resulting from multiple-path interference in the context of nonlinear thermoelectricity in a two-terminal triangular triple-dot Aharonov-Bohm (AB) interferometer. We quantify the trade-off between efficiency and power in the nonlinear regime of our simple setup comprising three non-interacting quantum dots (two of them are connected to two reservoirs) placed at the vertex of an equilateral triangle and a magnetic flux Φ pierces it perpendicularly. For a spatially symmetric setup, we find that the optimal efficiency and power output can be obtained when the inter-dot tunneling strength is comparable to the dot-lead coupling, AB phase $\phi = \pi/2$, and few higher-order quantum interference patterns or harmonics are present. We find that the presence of higher harmonics is necessary but not sufficient to achieve optimal power output. The maximal constructive interference represented by three close-packed resonance peaks of the unit transmission can enhance the power output ($P_{max} \approx 2.35$ fW) almost 3.5 times as compared to the case where only a single channel participates in the transport, and the corresponding efficiency is about $0.80\eta_c$ where η_c is the Carnot efficiency. Geometric asymmetries and their effects on efficiency and power output are also investigated. An asymmetric setup characterized by the ratio of the coupling to the source and the drain terminals (x) can further enhance the maximum power output $P_{max} \approx 3.85$ fW for $x = 1.5$ with the same efficiency as that of the symmetric case.

PACS numbers: 85.25.Cp, 42.50.Dv

I. INTRODUCTION

Optimal conversion of heat to work is desirable for efficient energy harvesting technologies. The role of quantum coherence in efficient energy harvesting is an ongoing research area. Recent advancements in nanotechnology have enabled us to study quantum-dot thermoelectric heat machines where quantum interference effects can play an important role. A major difference between these thermoelectric-based machines and other machines is that they do not have any macroscopic moving parts (i.e., no turbines, pistons, etc.). Rather, the working principles of such nanoscale thermoelectric devices are based on the steady-state currents of microscopic particles (electrons, phonons, etc.). The steady-state conversion of heat to work at the nanoscale has been reviewed in various works [1–6]. Recent work on transport in photosynthetic chains reveals the positive role of quantum effects for enhanced energy transfer. It is well established that phase coherence and quantum effects dominate the behavior of nanoscale heat engines [7–12]. Numerous examples of heat engines using the quantum system as a working fluid have been proposed and even experimentally realized [2, 13, 14]. The Aharonov-Bohm (AB) rings offer a tunable system to study the role of quantum effects in heat and charge transport [15–17]. For three-terminal quantum-dot heat engines using an AB interferometer, it has been shown that the introduction of magnetic flux can enhance heat-to-work conversion [18, 19]. Quantum dot thermoelectric heat engines

based on a two-terminal Aharonov-Bohm interferometer exhibiting sizable thermopower and the figure of merit exceeding one in the linear and nonlinear regimes have been studied [12, 20]. Nonlinear thermoelectric transport in quantum systems has been studied using the scattering approach [3, 4]. Quantum mechanics places an upper bound on power output and efficiency at any power. The energy filtering mechanism can lead to maximum efficiency where the system allows only particles from a specific energy window to pass [3, 4]. The transmission function must be a sharply peaked boxcar function to obtain maximum efficiency. We find that the transmission function of approximate box car shape yet exhibits resonance peaks can deliver optimal power-efficiency configuration for moderate set-up asymmetries. The nonlinear thermoelectric transport in coupled nanostructures has been studied [21]. However, the interplay of internal coherent dynamics and coherent dot-lead coupling can give rise to a richer resonance structure. If the number of resonance peaks is equal to the number of transport channels such that each peak has unit transmission, then one can get enhanced power efficiency because of the maximal constructive interference. The role of such a higher-order interference pattern in thermoelectrics is relatively less explored.

In this perspective, nanoscale or low-dimensional materials are found to be one of the most encouraging candidates [22]. Typically, one considers a nanostructure made of a few quantum dots or a single-molecule junction between two thermal reservoirs maintained at different temperatures and electrochemical potentials. The quan-

tum interference between the background continuum of states and the discrete energy levels in the quantum dot leads to a formation of Fano resonance that is reflected as transmission asymmetries and is a measure of phase coherence [23, 24]. The role of Fano resonance in efficient heat-to-work conversion has been studied both theoretically and experimentally [25–30]. Quantum control of thermoelectric effects using Fano resonance has been investigated recently for a two-terminal single quantum-dot interferometer. Apart from the Fano resonance, the cyclic geometric arrangement of quantum dots can give rise to electron trajectories winding around the loop multiple times. One can manipulate this interference pattern using an external magnetic flux to get a maximal constructive interference pattern that facilitates efficient heat and charge transfer.

The imperative questions then arise: (i) can we engineer a transmission function to achieve maximal constructive interference? (ii) What is the role of higher-order interference patterns in efficient heat-to-work conversion? We answer these questions affirmatively.

In this work, we study the triple quantum-dot Aharonov-Bohm (AB) interferometer as a thermoelectric heat engine. We consider a triangular geometry with magnetic flux threading the loop and two reservoirs connected at the terminals, termed as the source and drain. The source and drain are maintained at temperatures T_S and T_D and chemical potentials μ_S and μ_D , respectively. To operate this setup as a thermoelectric heat engine we maintain $T_S > T_D$ and $\mu_S < \mu_D$. In addition, the operation of the heat engine in the non-linear regime is controlled by considering $\Delta T = T_S - T_D \gg (T_S + T_D)/2$ and $\Delta\mu = \mu_D - \mu_S \gg (\mu_D + \mu_S)/2$. The steady-state behavior of the model has been studied at zero temperature limits [31]. The discrete molecular symmetries of the triple-dot setup lead to richer transmission behavior and higher harmonics resulting from paths winding around the loop [32]. The higher harmonic modes are related to the periodicity of oscillation of electrons' waves propagating through the AB ring by Φ_0/n , where $\Phi_0 = h/e$ is the flux quantum and n is the number of circulations around the AB ring. The role of these higher harmonics has been studied theoretically [33] and experimentally [34–37]. It has been proposed that the smallest and simplest ring to observe the higher harmonics is a molecule of three sites in a triangular arrangement embedded with quantum dots [38]. The effects of such higher-order interference patterns on the performance of thermoelectric heat engines are relatively less explored. This work explores the role of higher-order harmonics (higher-order quantum interferences) in efficient heat-to-work conversion. The central findings of our work are as follows:

- The presence of higher-order harmonics is necessary but not sufficient for the optimal power-efficiency configuration.
- The presence of multiple sharply peaked and equally spaced resonances of unit transmission

around the dot energy is crucial to achieving optimal power output. The output power is reduced in the presence of a single resonance transmission peak when the inter-dot tunneling strength t is much less than the dot lead hybridization strength γ although the efficiency is very high.

- For $\gamma = t$ and $t > \gamma$ regimes, the transmission function always exhibits three peaks. The area under the transmission curve is larger compared to the $\gamma > t$ regime. The larger area under the curve means more energy states are within the transport window. All channels participate in the transport and hence we get partially constructive interference. *The interference pattern becomes maximally constructive for $\phi = \pi/2$ where we observe the most optimal power-efficiency configuration.*
- We obtain the optimal power-efficiency configuration when $t = \gamma$. In this regime, the time scale of winding around the loop (which gives rise to higher-order harmonics) is comparable to the rate at which electrons exit the loop. We obtain three transmission peaks of unit transmission and two dips with a transmission nearly equal to half. In this case, all three channels participate in transport and the system acts like a coherent beam splitter exhibiting maximal constructive interference.
- We further find that the presence of anti-resonances, that gives rise to destructive interference channels reduces both the power output and efficiency. This is evidenced in the $t > \gamma$ regime, where the three sharp peaks move further apart and the anti-resonance dips start to develop. The reduction in power and efficiency can be attributed to the phenomena of localization where the electron spends more time within the triple-dot loop (winding over the loop dominates over the exit from the loop).
- For symmetric and low to moderate asymmetric cases, we find that the power is optimal for $\phi = \pi/2$. In this case, the triple-dot exhibits maximal constructive interference, leading to enhanced power output.
- For the moderate to low set-up asymmetries characterized by the ratio of coupling to the source and drain terminals, the power output is enhanced by 1.5 times as that of the symmetric case. For these cases, we can retain three peak transmission structures. Increasing the asymmetry parameter further leads to the reduction of the power output.

The organization of our paper is as follows: We first describe our model and the formalism in Sec. II. We analyze the density of states (DOS) and transmission function properties of our model set up in the fully non-linear regime in Sec. III. Section IV is devoted to the

thermoelectric power and thermodynamic conversion efficiency of our setup and their tunability with magnetic flux, gate voltage, temperature bias, and dot-lead coupling strength. The connection between power-efficiency behavior and the harmonics of particle current and heat current for three different regimes demarcated by the parameter t/γ (t is the interdot tunneling strength and γ is the hybridization strength) : (a) $t/\gamma < 1$ (b) $t/\gamma \sim 1$ and (c) $t/\gamma > 1$. Our analysis shows that regime (b) with $\phi = \pi/2$ is the most optimal region for the operation of our thermoelectric engine. In Sec. V we discuss the role of the geometry of the triple-dot setup for enhanced thermoelectric response. We conclude our paper in Sec. VI.

II. MODEL HAMILTONIAN AND FORMALISM

We consider a model setup of a triple-quantum-dot Aharonov-Bohm (AB) interferometer [31, 39–42], as shown in Fig. 1(a). Here, each quantum dot is located at the vertex of an equilateral triangle and interconnected to each other by quantum tunneling. A magnetic flux Φ pierces the triangular AB ring perpendicularly. Dot 1 and dot 3 are connected to two metallic leads (bath or reservoir) maintained at different temperatures and chemical potentials. Here we do not consider the electron-electron interactions and the spin degrees of freedom to construct a simple solvable setup. Hence we can describe quantum dots by a spin-less electronic level and ignore the Zeeman effect. The total Hamiltonian \hat{H} of the whole system is given by,

$$\hat{H} = \hat{H}_{TQD} + \hat{H}_B + \hat{H}_{TQD,B}, \quad (1)$$

where \hat{H}_{TQD} is the Hamiltonian for the three quantum dots (subsystem), \hat{H}_B is the Hamiltonian for the metallic leads (bath), and $\hat{H}_{TQD,B}$ is the interaction Hamiltonian between the subsystem and the baths. The subsystem Hamiltonian consisting of three interconnected dots is given as

$$\hat{H}_{TQD} = \sum_{i=1,2,3} \epsilon_i \hat{d}_i^\dagger \hat{d}_i + \left[\sum_{i \neq j} t_{ij} \hat{d}_i^\dagger \hat{d}_j e^{i\phi_{ij}} + \text{h.c.} \right]. \quad (2)$$

Here, ϵ_i denotes the energy of the i th dot. \hat{d}_i^\dagger and \hat{d}_i are the creation and annihilation operators of the electrons in the respective dots and t_{ij} is the inter-dot tunneling strength and ϕ_{ij} is the AB phase factor. The Hamiltonian for the two metallic leads, source (S) and drain (D), consisting of noninteracting electrons is

$$\hat{H}_B = \sum_{k, \nu \in S, D} \epsilon_{\nu,k} \hat{c}_{\nu,k}^\dagger \hat{c}_{\nu,k}, \quad (3)$$

where $\hat{c}_{\nu,k}^\dagger$ and $\hat{c}_{\nu,k}$ represents the creation and annihilation operators of the electrons in the k th momentum state and $\epsilon_{\nu,k}$ is the energy of the k th state in the corresponding baths, $\nu \in S, D$. Since dot 1 is connected to the

source (S) and dot 3 is connected to the drain (D), we can write the subsystem-bath interaction term as follows

$$\hat{H}_{TQD,B} = V_{1,k}^S \hat{d}_1^\dagger \hat{c}_{S,k} + V_{3,k}^D \hat{d}_3^\dagger \hat{c}_{D,k} + \text{h.c.} \quad (4)$$

Here $V_{i,k}^\nu$ denotes the dot-bath coupling strength. The AB phases ϕ_{ij} satisfy the following relation [31],

$$\phi_{12} + \phi_{23} + \phi_{31} = \phi = 2\pi \frac{\Phi}{\Phi_0}, \quad (5)$$

where Φ is the total magnetic flux enclosed by the triangular AB ring and $\Phi_0 = h/e$ is the flux quantum. In the steady state, physical observables are gauge invariant. Since the dots are present at the vertices of an equilateral triangular loop, we may choose the gauge as $\phi_{12} = \phi_{23} = \phi_{31} = \phi/3$. For our system, we maintained a symmetric voltage bias condition i.e., $\mu_S = -\mu_D$. Although, by applying a gate voltage to each dot we can place the levels of the dots away from the symmetric point at which $\mu_S - \epsilon_i = \epsilon_i - \mu_D$. For simplicity, we use the natural unit convention $\hbar = c = e = k_B = 1$. We translate our results to physical units in Appendix B.

A. Non-equilibrium Green's functions for the AB interferometer setup

To solve this model and compute the observables of interest, we use the Nonequilibrium Green's Function (NEGF) approach [43–45]. We follow the equation of motion method for the calculations (for details see Appendix A) and obtain the retarded $[G^+(\omega)]$ and advanced $[G^-(\omega)]$ Green's function for our system by using the quantum Langevin equation [46]. The Green's functions are given as,

$$G^\pm(\omega) = \left[\omega I - H_{TQD} - \Sigma_S^\pm(\omega) - \Sigma_D^\pm(\omega) \right]^{-1}, \quad (6)$$

where I is a (3×3) identity matrix. Here $\Sigma_S^\pm(\omega)$ and $\Sigma_D^\pm(\omega)$ are the self-energies defined in Eq. (A8) of Appendix A. H_{TQD} is the single particle matrix corresponding to the Hamiltonian \hat{H}_{TQD} in Eq. (2) and given by,

$$H_{TQD} = \begin{pmatrix} \epsilon_d & te^{i\phi/3} & te^{-i\phi/3} \\ te^{-i\phi/3} & \epsilon_d & te^{i\phi/3} \\ te^{i\phi/3} & te^{-i\phi/3} & \epsilon_d \end{pmatrix}. \quad (7)$$

Note that, we impose energy degeneracy for the dots $\epsilon_1 = \epsilon_2 = \epsilon_3 = \epsilon_d$ and further consider identical symmetric inter-dot tunneling strength as $t_{12} = t_{23} = t_{13} = t$. In the wide-band limit when the density of states of the metallic lead is energy independent, the real part of the self-energy term vanishes. Then we can define the hybridization matrix from the relation $\Sigma^+ = -i\Gamma/2$:

$$\Gamma_{i,i'}^\nu = 2\pi \sum_{k,\nu} V_{i',k}^{\nu*} V_{i,k}^\nu \delta(\omega - \omega_k). \quad (8)$$

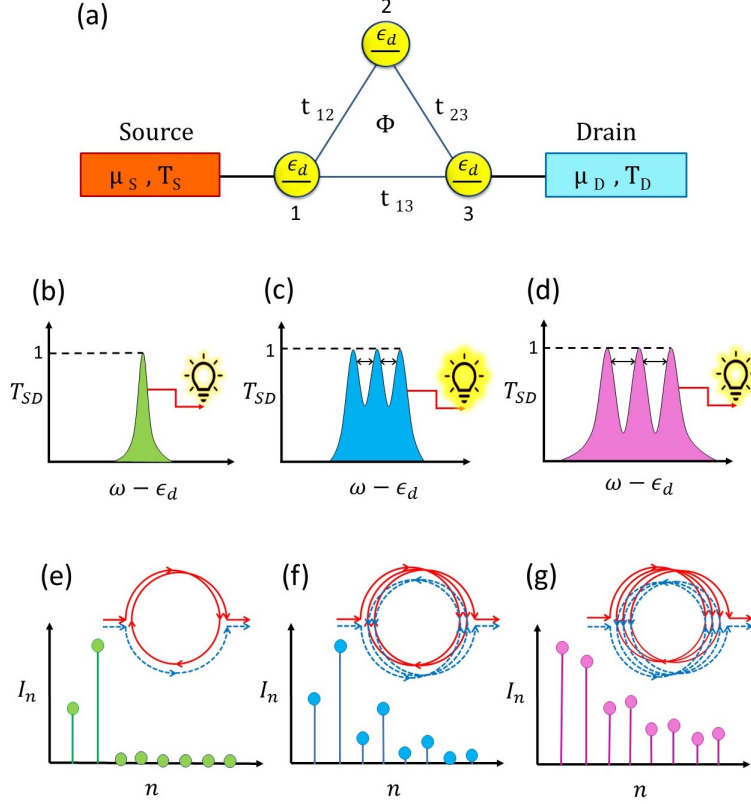


FIG. 1. (a) A triple quantum dot Aharonov-Bohm interferometer with dot 1 and dot 3 connected to source and drain, respectively. A magnetic flux Φ pierces the triangular AB ring perpendicularly. Figures (b)-(d) show transmission patterns with respect to energy. (b) A single symmetric peak around resonance is more efficient but generates less power. (c) We need three peaks equally spaced around the resonance to achieve optimal power and efficiency as shown in the figure with the brightest bulb. (d) When the separation between the peaks increases antiresonance is more pronounced causing a decrease in power and efficiency. The bottom set of figures shows harmonic patterns of charge current obtained by Fourier decomposition with respect to ϕ ($n = 1, 2, 3, \dots$), and the different trajectories of the circulation of electrons around the AB ring are represented by blue and red orbits. The presence of higher harmonic modes is necessary but not sufficient to achieve optimal power and efficiency. Figure (f) gives optimal power efficiency. (g) The dominance of higher harmonic modes is responsible for reducing efficiency.

We may take $V_{i,k}^\nu$ as real constants with $\nu = S, D$, independent of the level index and reservoir state, resulting in $\Gamma_{1,1}^S = \gamma_S$ and $\Gamma_{3,3}^D = \gamma_D$, where γ_ν describes the coupling between the dots and metallic leads and it is taken as a constant (energy independent).

We then receive the retarded Green's function as,

$$G^+(\omega) = \begin{pmatrix} \omega - \epsilon_d + i\frac{\gamma_S}{2} & -te^{i\phi/3} & -te^{-i\phi/3} \\ -te^{-i\phi/3} & \omega - \epsilon_d & -te^{i\phi/3} \\ -te^{i\phi/3} & -te^{-i\phi/3} & \omega - \epsilon_d + i\frac{\gamma_D}{2} \end{pmatrix}^{-1}. \quad (9)$$

The hybridization matrices are given by

$$\Gamma^S = \begin{pmatrix} \gamma_S & 0 & 0 \\ 0 & 0 & 0 \\ 0 & 0 & 0 \end{pmatrix}, \Gamma^D = \begin{pmatrix} 0 & 0 & 0 \\ 0 & 0 & 0 \\ 0 & 0 & \gamma_D \end{pmatrix}. \quad (10)$$

We can define the advanced Green's function as conjugate transpose matrix $G^-(\omega) = [G^+(\omega)]^\dagger$. The details are discussed in Appendix A.

B. Observables: Currents, Output Power and Efficiency

It is of interest to investigate the subsystem properties and obtain the transmission coefficient, particle currents, and heat currents through the system. The transmission of electrons from reservoir ν to ξ is given by the transmission coefficient [47]

$$T_{\nu\xi}(\omega, \phi) = \text{Tr}[\Gamma^\nu G^+(\omega, \phi) \Gamma^\xi G^-(\omega, \phi)]. \quad (11)$$

Using the transmission coefficients $T_{\nu\xi}$, we can express the particle currents flowing from reservoir ν to the cen-

tral system as [48, 49]

$$I_\nu = \int_{-\infty}^{\infty} d\omega \sum_{\xi \neq \nu} [T_{\nu\xi}(\omega, \phi) f_\nu(\omega) - T_{\xi\nu}(\omega, \phi) f_\xi(\omega)]. \quad (12)$$

Similarly, the heat current from the reservoir ν is given by

$$Q_\nu = \int_{-\infty}^{\infty} d\omega (\omega - \mu_\nu) \sum_{\xi \neq \nu} [T_{\nu\xi}(\omega, \phi) f_\nu(\omega) - T_{\xi\nu}(\omega, \phi) f_\xi(\omega)], \quad (13)$$

where $f_{\nu(\xi)}(\omega) = [e^{(\omega - \mu_{\nu(\xi)})/T_{\nu(\xi)}} + 1]^{-1}$ is Fermi distribution function of the reservoir $\nu(\xi) = S, D$ with μ_ν and T_ν be the corresponding chemical potential and temperature, respectively.

To characterize the nonlinear thermoelectric performance of a two-terminal system as a heat engine, we shall study the output power P and the steady-state heat-to-work conversion efficiency η . Our model uses the configuration $\Delta\mu = \mu_D - \mu_S > 0$ and $\Delta T = T_S - T_D > 0$. The output power P is equal to the sum of all the heat currents exchanged between the subsystem and the reservoir and it is given by [1, 50]

$$P = \sum_{\nu=S,D} Q_\nu = (\mu_D - \mu_S) I_S. \quad (14)$$

Equation (14) follows the laws of conservation of particle $\sum_\nu I_\nu = 0$ and energy. We define the efficiency η as the ratio of output power P to the heat currents absorbed from the hot bath and it is expressed as [1, 50]

$$\eta = \frac{P}{Q_S}. \quad (15)$$

The system work as a heat engine for positive output power $P > 0$ with positive heat current flow from the source $Q_S > 0$. The efficiency η is bounded from the above by Carnot efficiency $\eta_C = 1 - T_c/T_h$ with T_c and T_h being the temperatures of cold and hot baths, respectively [51].

III. TRANSPORT PROPERTIES: DENSITY OF STATES AND TRANSMISSION FUNCTION

In this section, we analyze the interrelationship between the density of states (DOS) and the system's transmission function, which gives information about the transport properties, for symmetric dot-lead coupling strength i.e., $\gamma_S = \gamma_D = \gamma$. Since we are interested in the transport properties of the AB interferometer, the effect of magnetic flux ϕ , and the ratio t/γ become crucial in this analysis. The ratio t/γ demarcates three different regimes for our analysis : (i) $t < \gamma$ region, (ii) $t \sim \gamma$ region, and (iii) $t > \gamma$ region.

The density of states (DOS) is given by the trace of

the imaginary part of the retarded Green's function as [47]

$$D(\omega, \phi) = -\frac{1}{\pi} \text{Tr}[\text{Im}(G^+)], \quad (16)$$

which for our setup is given as,

$$D(\omega, \phi) = \frac{\gamma}{\pi \Delta(\omega, \phi)} \left[(\omega - \epsilon_d)^4 + \frac{\gamma^2}{4} (\omega - \epsilon_d)^2 + 4t^3 \cos \phi (\omega - \epsilon_d) + t^2 (3t^2 + \frac{\gamma^2}{4}) \right], \quad (17)$$

where

$$\Delta(\omega, \phi) = \left[(\omega - \epsilon_d) \left((\omega - \epsilon_d)^2 - 3t^2 - \frac{\gamma^2}{4} \right) - 2t^3 \cos \phi \right]^2 + \gamma^2 \left[(\omega - \epsilon_d)^2 - t^2 \right]^2. \quad (18)$$

We can express the transmission function from reservoir S to D with symmetric dot-lead coupling ($\gamma_S = \gamma_D = \gamma$) analytically as

$$T_{SD}(\omega, \phi) = \frac{\gamma^2 [t^4 + 2t^3 \cos \phi (\omega - \epsilon_d) + t^2 (\omega - \epsilon_d)^2]}{\Delta(\omega, \phi)}. \quad (19)$$

For $\phi = \pi/2$, the transmission peaks [$T_{SD}(\omega, \phi) = 1$] are at positions

$$\omega = \epsilon_d, \quad \text{and} \quad \omega = \epsilon_d \pm \frac{1}{2} \sqrt{12t^2 - \gamma^2}. \quad (20)$$

Equation 20 is valid in all the regimes except when $t \ll \gamma$, where we have a single transmission peak at $\omega = \epsilon_d$. We have three transmission peaks at energies given by Eq. (20) for all other cases.

Considering our model set-up where the triple-dot AB interferometer is connected to two reservoirs or leads, the transmission function describes the quantum interference. The transmission function can exhibit both constructive and destructive interference. Further, we observe that DOS is directly related to the transmission function. We analyze this quantity for the three different regimes. In Fig. 2(a1), for $t < \gamma$, we observe an asymmetric structure in DOS with energy when the magnetic flux is zero i.e., $\phi = 0$. As we change the flux to $\phi = \pi/4$ and $\pi/2$, the asymmetry vanishes and we get a single peak (see Fig. 2(a2), (a3)). We can also see this behavior in the transmission function. We observe an asymmetric antiresonance dip in transmission at $\phi = 0$ as shown in Fig. 2(b1) and as we increase the magnetic flux to $\phi = \pi/2$ the asymmetry in transmission vanishes and we get a single peak symmetric around $\omega = \epsilon_d$ (see Fig. 2(b3)). It has also been observed that the DOS and transmission function behavior for $\phi = \pi$, $\phi = 3\pi/4$ has reflection symmetry of that of $\phi = 0$ and $\phi = \pi/4$, respectively. This is also true for other values of ϕ .

In the $t \sim \gamma$ regime, we can observe that the DOS

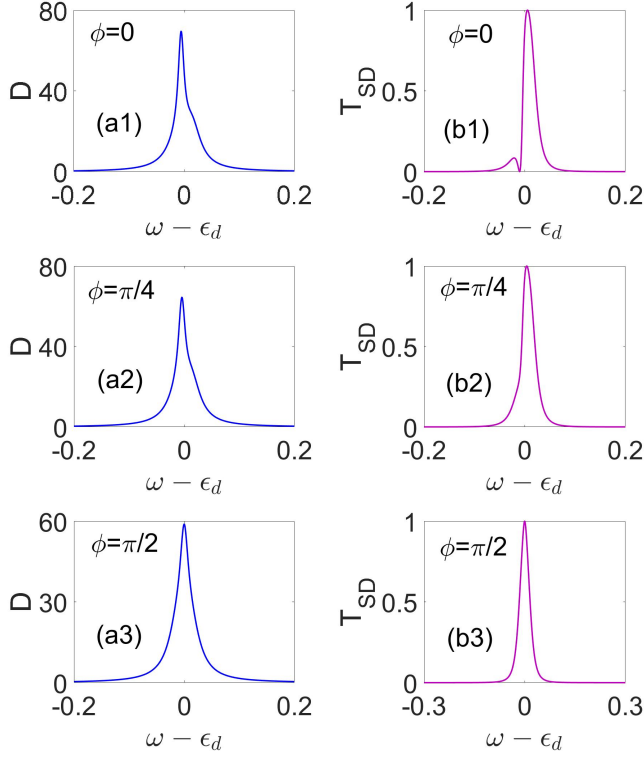


FIG. 2. Density of states (a1-a3) and transmission functions (b1-b3) as a function of energy at different values of ϕ for $t < \gamma$ regime. Parameters used are $\gamma = 0.05$, $t = 0.2\gamma$, $\epsilon_d = 8\gamma$, $T_S = 12\gamma$, $T_D = 2\gamma$, $\mu_S = -4\gamma$, $\mu_D = 4\gamma$.

has two peaks and the transmission has antiresonance dip for $\phi = 0$ in Fig. 3(b1). Further, as we change the magnetic flux from $\phi = 0$ to $\phi = \pi/4$ the DOS and the transmission function exhibit three resonance peaks. For $\phi = \pi/2$, resonance peaks become sharper and are symmetrically situated around $\omega = \epsilon_d$ (see Fig. 3(b3)) such that the maximum transmission is one and the minimum is half. It opens up more transport channels and all three states participate equally in transport for $\phi = \pi/2$, $t = \gamma$ leading to perfectly constructive interference. For the $t > \gamma$ regime as shown in Fig. 4, we observe that the DOS and transmission function show a double resonance peak for $\phi = 0$. As one increases ϕ , we observe the splitting of the peaks of the DOS and transmission function. One can observe three equally spaced resonance peaks for $\phi = \pi/2$ symmetric around ϵ_d . The separation between the resonance peaks becomes wider for both DOS and the transmission function and it is accompanied by two deep antiresonance dips as compared to the $t = \gamma$ regime.

From the above analysis, we can conclude that the behavior of the transmission function and the density of states are identical. This suggests a peculiar way of engineering quantum-dot structures to achieve the maximal constructive interference condition. We can explain the antiresonance dip in transmission i.e., $T_{SD} = 0$ for $\phi = 0$

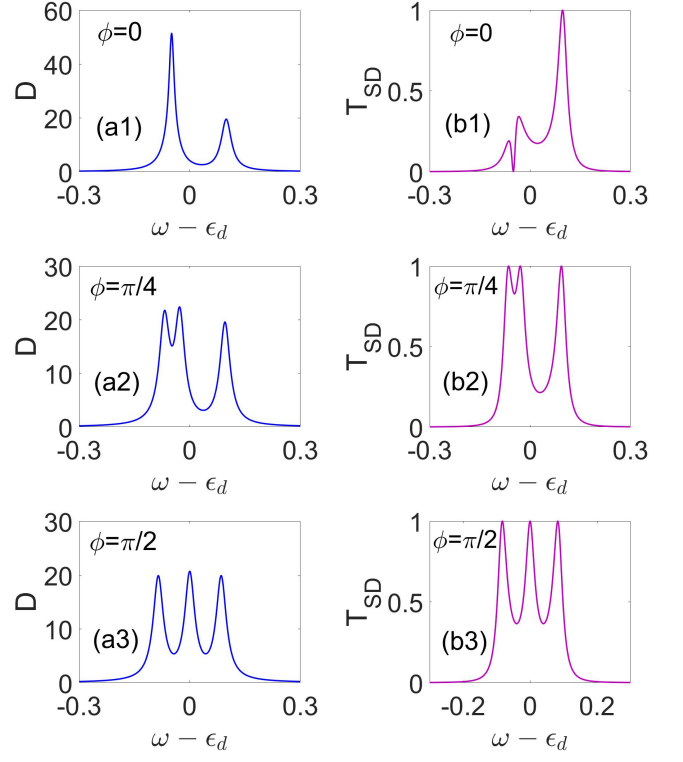


FIG. 3. Density of states (a1-a3) and transmission functions (b1-b3) as a function of energy at different values of ϕ for $t = \gamma$ regime. Parameters used are $\gamma = 0.05$, $t = \gamma$, $\epsilon_d = 8\gamma$, $T_S = 12\gamma$, $T_D = 2\gamma$, $\mu_S = -4\gamma$, $\mu_D = 4\gamma$.

in all the three regimes from the energy spectrum of the isolated triple-dot AB setup. The strong (compared to lead-dot coupling) inter-dot tunneling coupling leads to a strong hybridization between triple-dot states. Owing to the discrete molecular symmetry of the setup, the spectrum exhibits degeneracies depending on the magnetic flux values. In the case of an isolated symmetric triple dot, it can be shown that the energy eigenstates are Bloch waves uniformly delocalized over three sites. When a pair of degenerate levels is in resonance with incoming electrons from leads, the transmission probability vanishes which is a consequence of destructive interference. These states are known as ‘dark states’. Further, if the contact with the lead is weak, then the energy-level structure of the isolated triple-dot will be reflected in the plot of the transmission function, and T_{SD} will possess a series of peaks depending on the energy of the incoming electron located at energies in the vicinity of the energy spectrum. We observe this behavior from $t \sim \gamma$ and $t > \gamma$ regimes from Fig. 3 and Fig. 4, respectively. But the separation between the resonance peaks becomes wider and antiresonance dips become broader as we move from $t \sim \gamma$ to $t > \gamma$. We observe a perfectly constructive interference for $\phi = \pi/2$, $t \sim \gamma$ and each state contributes equally to the transport. This is analogous to an almost loss-free beam splitter where the transmission through each chan-

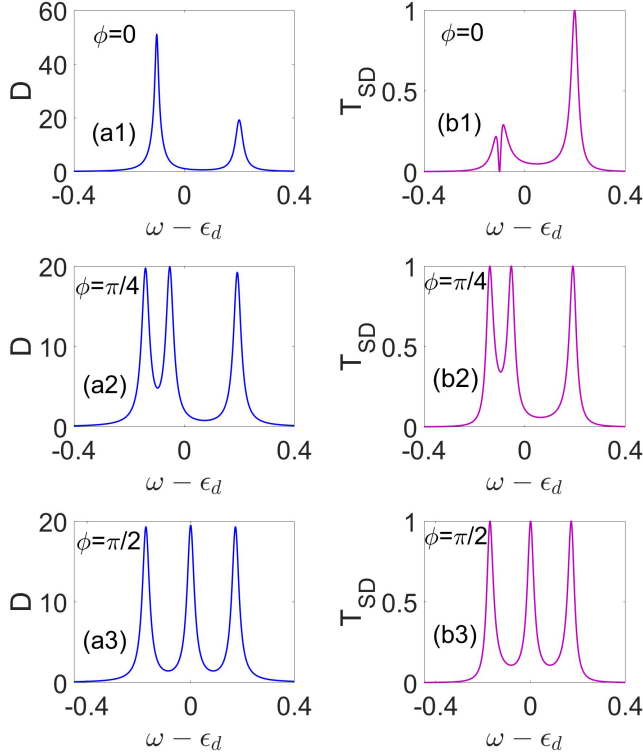


FIG. 4. Density of states (a1-a3) and transmission functions (b1-b3) as a function of energy at different values of ϕ for $t > \gamma$ regime. Parameters used are $\gamma = 0.05$, $t = 0.2\gamma$, $\epsilon_d = 8\gamma$, $T_S = 12\gamma$, $T_D = 2\gamma$, $\mu_S = -4\gamma$, $\mu_D = 4\gamma$.

nel is unity. This would facilitate efficient charge and energy transport. To achieve optimal power efficiency, the maximum transmission should be one and the minimum should be half. The presence of antiresonance dips reduces efficiency. In the subsequent section, we observe that the position of these transmission peaks and their separation is crucial for the power-efficiency trade-off for a thermoelectric heat engine. We also study the efficiency of the heat engine and connect it with multiple-harmonics patterns which can be extracted from the Fourier analysis of the steady-state charge and heat currents.

IV. POWER-EFFICIENCY TRADE-OFF AND ANALYSIS OF HARMONICS IN CURRENTS

In this section, we analyze the power versus efficiency trade-off in the nonlinear regime as a function of the magnetic flux ϕ and the ratio of the intra-dot tunneling rate t and the hybridization strength γ i.e., t/γ . Considering a particular temperature bias, we find the optimal flux and ratio t/γ to maximize both output power and efficiency as defined in Eqs. (14) and (15), respectively. We demonstrate the Lasso-type parametric plot of efficiency versus power and verify the trade-off between both quantities. We demonstrate that the AB heat engine can be tuned through external magnetic flux ϕ , gate voltage V_g

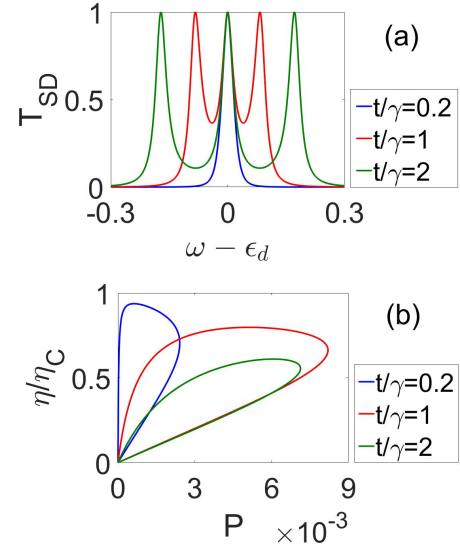


FIG. 5. (a) Transmission function and (b) Power-efficiency diagram for different values of tunneling strength t . Parameters used are $\gamma = 0.05$, $\epsilon_d = 8\gamma$, $\mu_S = -\mu_D$, $T_S = 12\gamma$, $T_D = 2\gamma$, $\phi = \pi/2$.

(to vary the dot energy), temperature bias ΔT , and the ratio t/γ to optimize either efficiency or power or the both.

From Fig. 5(b), it is observed that we get the maximum efficiency for $t < \gamma$, but at the cost of low power output. In this case, we can see that the transmission has less area under the curve, and a single channel participates in the transport. For the $t = \gamma$ regime, we get maximum output power with a larger efficiency. For this case, we find that three resonances are closer and equally contribute. In this regime, irrespective of ϕ , we find that there are three peaks (not necessarily equally spaced) in the transmission, and we observe the higher harmonics. The magnitude of these harmonics also increases as we move from $\gamma > t$ to $\gamma = t$. We can conclude that $t \sim \gamma$ and $\phi = \pi/2$ is the optimal regime for transport where the transmission function has three peaks with equal separation as shown in Fig. 5(a). Three peak structure of the transmission signals the higher-order interference pattern arising from trajectories winding multiple times within the triple-dot subspace. There is only one transport channel for $t < \gamma$, and the transmission peaks start separating as we move from the $t < \gamma$ regime towards $t \sim \gamma$ regime. The separation between the three resonance peaks becomes wider, and the antiresonance is more pronounced as we move from $t \sim \gamma$ to $t > \gamma$ regime. In the $t > \gamma$ regime, inter-dot tunneling is very large compared to the dot-lead hybridization strength. Thus, the electrons which are coming from the source will prefer to circulate in the loop and hence efficiency decreases although power output is still much larger than the $\gamma > t$ case.

The above observations can be further understood

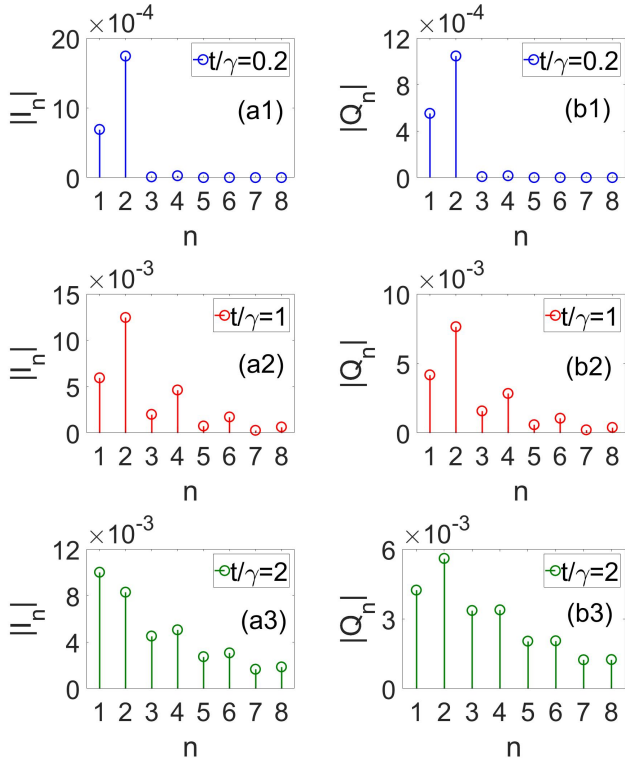


FIG. 6. (i) Harmonics for particle current from the source: (a1) $t/\gamma = 0.2$, (a2) $t/\gamma = 1$, and (a3) $t/\gamma = 2$; (ii) Harmonics for heat current from the source: (b1) $t/\gamma = 0.2$, (b2) $t/\gamma = 1$, and (b3) $t/\gamma = 2$. Parameters used are $\gamma = 0.05$, $\epsilon_d = 8\gamma$, $\mu_D = -\mu_S = 4\gamma$, $T_S = 12\gamma$, $T_D = 2\gamma$. Irrespective of ϕ , the higher harmonics are non-zero for $t/\gamma = 1$ and $t/\gamma \geq 1$.

with the help of harmonic analysis of the particle and heat currents. One can analyze it as described below: The Aharonov-Bohm oscillations of charge current have a periodicity equal to $\Phi_0 = h/e$. However, higher harmonics with periodicity Φ_0/n can also be observed with $n \geq 2$. These higher harmonics can be related to the circulation of electrons n times in the triple-dot ring [32]. We define the harmonics for the particle current as

$$I_n = \int_0^{2\pi} d\phi I(\phi) e^{in\phi}. \quad (21)$$

Similarly, the harmonics for the heat current can be defined as

$$Q_n = \int_0^{2\pi} d\phi Q(\phi) e^{in\phi}, \quad (22)$$

where $\phi = 2\pi\Phi/\Phi_0$. Here $I(\phi)$ and $Q(\phi)$ are the expression for particle current and heat current from the source as discussed in Eqs. (12) and (13), respectively.

It has been observed that the formation of the localized dark state in this triple-dot setup always leads to the $n = 2$ harmonic dominance [52–58]. Here we observe that only the first two harmonic modes (mostly the second harmonic) are dominating for the strong coupling

case ($t < \gamma$) as shown in Fig. 6(a1) and 6(b1). In this regime, the transmission has a single peak at $\omega = \epsilon_d$ i.e., only one state on a resonance that participates in the transport. This leads to the high efficiency of the system but low power output. Since the electrons coming from the source can circulate in the loop only once or twice and exit from the loop to the drain. We find that the $t \sim \gamma$ regime is the optimal regime for the operation of the thermoelectric heat engine. Since some of the higher harmonics ($n > 2$) are also contributing to this regime. Here all three states contribute to the transport. The output power is enhanced as the magnitude of the charge and heat current harmonics increases as shown in Figs. 6(a2) and 6(b2), respectively. There is a balance between efficiency and output power in this region. *In other words, the time scale of internal coherence dynamics of the triple dot should be comparable to the rate at which the triple dot state decays to the source and or drain terminal to achieve higher power output.* In the weak coupling region, $t > \gamma$, all the higher harmonics contribute considerably. Hence the efficiency and output power are reduced as compared to the $t \sim \gamma$ regime. We can see that the magnitude of the higher harmonics is still comparable, but the first harmonics of the charge current are greater in magnitude than that of the heat current. This lag between harmonics results in lower efficiency for $t > \gamma$ regime.

Figure 7 shows the trade-off between the output power and efficiency for different values of magnetic flux ϕ in three different regimes of t . It is observed that for all the three regimes of t , we get maximum output power at $\phi = \pi/2$ and the power is comparably less at $\phi = 0$. This can be explained by the transmission function behavior that we observe as an antiresonance dip as shown in Figs. 2(b1), 3(b1) and 4(b1). Two symmetric resonance peaks around ϵ_d for $\phi = \pi/2$ open up more transport channels for charge and energy transport that gives optimal power efficiency configuration.

From the above analysis, we can conclude that the presence of three resonance peaks with optimal separation between them is crucial for obtaining optimal output power and efficiency as in the case of $t \sim \gamma$. The presence of antiresonance dips in the $t > \gamma$ regime causes a reduction in both output power and efficiency. The harmonic analysis in Fig. 6 helps us understand the role of higher harmonic modes in enhancing thermoelectric performance. The contribution of higher harmonics is necessary for obtaining optimal output power but is not sufficient. When there is a more significant contribution from higher harmonic modes and the electrons spend more time circulating the loop rather than exiting the loop, then there is a reduction in efficiency and output power. We need a balance between the harmonics of both particle current and heat current to obtain optimal power output and efficiency. Also, we investigate the tunability of the thermoelectric performance of our model with the magnetic flux. The triple-dot exhibits

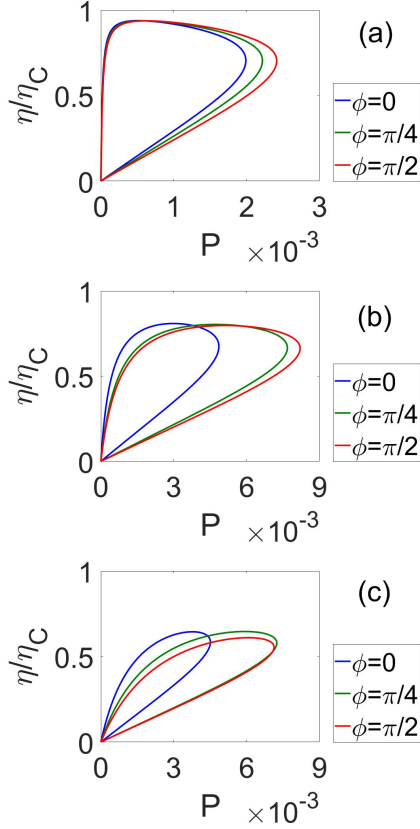


FIG. 7. Power-efficiency diagram for different values of ϕ at (a) $t/\gamma = 0.2$, (b) $t/\gamma = 1$, (c) $t/\gamma = 2$. Other parameters are $\gamma = 0.05$, $\epsilon_d = 8\gamma$, $\mu_D = -\mu_S$, $T_S = 12\gamma$, $T_D = 2\gamma$.

maximum constructive interference at $\phi = \pi/2$ and we obtain maximum output power at $\phi = \pi/2$ for all the three regimes of t . With this analysis, we can conclude that $t \sim \gamma$ and $\phi = \pi/2$ are the optimal configurations to reach maximum output power and efficiency. In the following section, we study the power-efficiency behavior for a geometrically asymmetric setup with dissimilar dot-lead coupling strength.

V. POWER-EFFICIENCY TRADE-OFF FOR ASYMMETRIC SETUPS

Real experimental systems can exhibit asymmetries arising from imperfections in fabrications and/or disorder. Therefore, it is instructive to investigate the effects of geometric asymmetries on power-efficiency behavior. We can introduce asymmetry to our system by introducing asymmetric dot-lead coupling strength ($\gamma_S \neq \gamma_D$). Let us define the asymmetric parameter as $x = \gamma_S/\gamma_D$. We discuss asymmetric behavior in the following section.

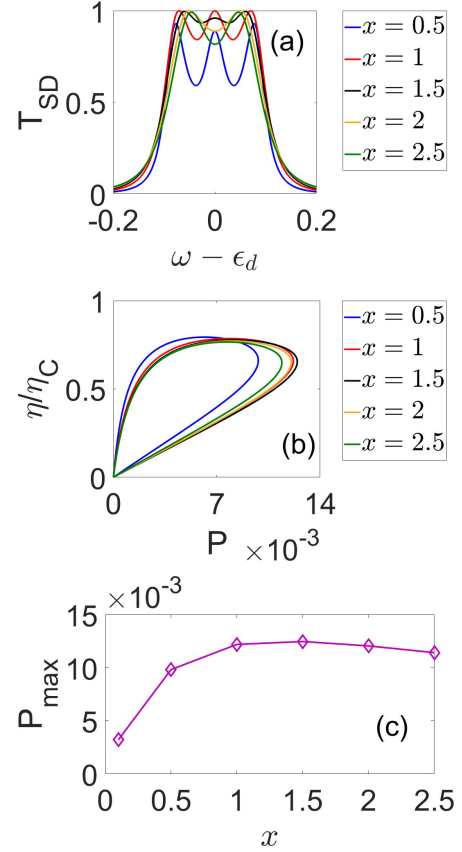


FIG. 8. (a) Transmission function, (b) Power-efficiency diagram for asymmetric dot-lead coupling, and (c) maximum output power (P_{max}) as a function of asymmetric dot-lead coupling ratio. Parameters used $\gamma_D = 0.1$, $t = 0.5\gamma_D$, $\epsilon_d = 4\gamma_D$, $\phi = \pi/2$, $\mu_D = -\mu_S$, $T_S = 6\gamma_D$, $T_D = \gamma_D$.

A. Asymmetric dot-lead coupling strength

The power and efficiency of our heat engine model, also depend on the asymmetric dot-lead coupling strength (see Fig.8). For the AB thermoelectric heat engine, it seems that an asymmetric coupling between the source-system, γ_S , and drain-system, γ_D , is also helpful to manipulate either efficiency or the power or both. Figure 8 shows the transmission function and power-efficiency behavior for different asymmetric ratios x . Considering fixed values of the other parameters, we can achieve maximum efficiency up to 0.8 of Carnot efficiency by adjusting the asymmetric parameter x . By increasing the asymmetric parameter the maximum output power (P_{max}) increases from $x = 0.5$ up to $x = 1.5$ and then P_{max} decreases by further increasing the asymmetric parameter for $x = 2$ and $x = 2.5$ as evidenced in Fig.8(b) and Fig.8(c). This can be explained by the transmission functions in Fig.8(a). For $x = 0.5, 1, 1.5$, there are three resonance transmission peaks. As the antiresonance dips are more significant for $x = 0.5$, the maximum output power is less as compared to $x = 1$ and the antiresonance

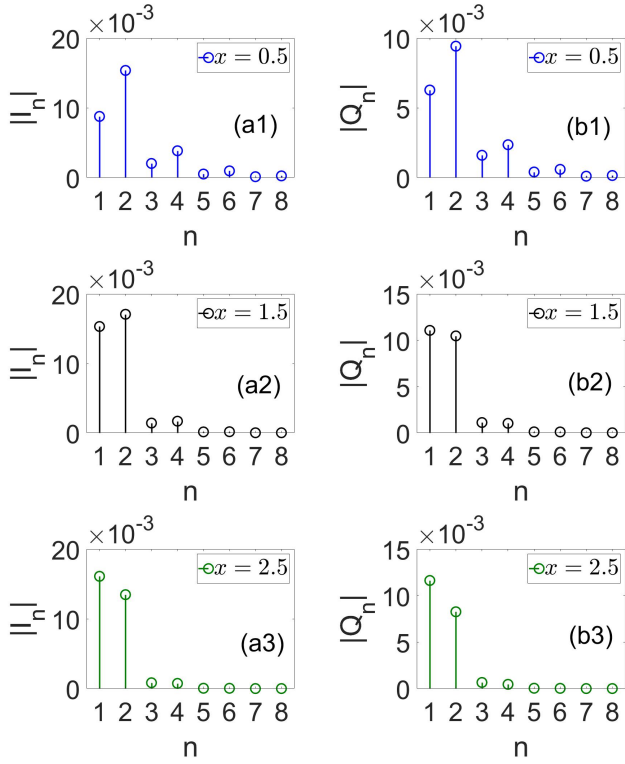


FIG. 9. (i) Harmonics for particle current from the source: (a1) $x = 0.5$, (a2) $x = 1.5$, and (a3) $x = 2.5$; (ii) Harmonics for heat current from the source: (b1) $x = 0.5$, (b2) $x = 1.5$, and (b3) $x = 2.5$ for asymmetric dot-lead coupling. Parameters used $\gamma_D = 0.1$, $t = 0.5\gamma_D$, $\epsilon_d = 4\gamma_D$, $\phi = \pi/2$, $\mu_D = -\mu_S = 2\gamma_D$, $T_S = 6\gamma_D$, $T_D = \gamma_D$.

dips are least significant for $x = 1.5$ at which we obtain maximum output power $P_{max} = 0.0125$. For $x = 2$ and $x = 2.5$, the three resonance transmission peaks merge to form two peaks causing a reduction of output power with antiresonance dips being more significant for $x = 2.5$ which further reduces the maximum output power. So, by observing Fig. 8, we can conclude that whenever there are three peaks and the antiresonance dips are not much significant (i.e., $x = 1.5$), we will get maximum output power. Figure 9 shows the harmonic modes for particle current and heat current at different asymmetric parameters i.e., $x = 0.5$, $x = 1.5$, and $x = 2.5$. This procedure does not reflect the absolute optimal values of power and efficiency as a function of all parameters of interest in possible experimental realizations, rather it demonstrates the high tunability of the AB interferometer as a heat engine to achieve a high amount of power and efficiency in the quantum regime.

VI. DISCUSSION

To conclude, we demonstrated a transmission engineering of a triple-dot Aharonov-Bohm interferometer to give an optimal power-efficiency configuration. We find

that the higher-order interference patterns from multiple paths winding around the loop are necessary but insufficient for the optimal power-efficiency configuration. If there is a sufficiently strong hybridization of triple-dot molecular states such that the time-scale of internal coherent dynamics (dictated by $1/t$) is comparable to the dot-lead hybridization strength, then we obtain three transmission peaks with transmission probability one and the two dips with the transmission probability one-half, then there is a maximally constructive interference effect that boosts the power-efficiency. In the present set-up, this condition is satisfied for $\phi = \pi/2$. Further, by tuning $\gamma = t$, the three transmission peaks can be brought closer in energy. The central peak occurs at $\omega = \epsilon_d$, and the other two peaks occur at $\omega = \epsilon_d \pm \frac{1}{2}\sqrt{12t^2 - \gamma^2}$. For $\gamma = t$, $\omega = \epsilon_d \pm \frac{1}{2}\sqrt{11}t$ i.e peaks are closed for this case, and hence the constructive interference is achieved. By increasing t further, we observed that the peaks move apart and the anti-resonance dips start to develop thereby reducing the power and efficiency. We also examined the effects of set-up asymmetry and observed that low to moderate asymmetry can enhance the power output. In mesoscopic quantum-dot structures, the electron-electron interactions are not screened and therefore have to be taken into account beyond the mean-field description. This is a tedious task. But we can draw some qualitative insights into their effect on higher harmonics. First of all, in the non-interacting case, the charge and the heat currents are even functions of AB phase ϕ (owing to Onsager symmetry), and so $\cos(\phi)$ terms and their powers appear in the transmission probability. Incorporating the electron-electron interactions will break the even symmetry of charge and heat current. This will give rise to $\cos(\phi)$ and $\sin(\phi)$ terms which may suppress the harmonics beyond $n = 2$. This has already been observed for a Coulomb blockade and infinite bias case. We expect that the suppression of higher harmonics may also suppress the power-efficiency. But irrespective of many-body interactions and their form, we would like to point out that a peculiar structure of the transmission function is necessary so that maximal constructive interference can boost the power-efficiency of the engine.

The response of the present thermoelectric heat engine turns out to be significant. Particularly, the quantum device based on an AB interferometer can produce a sizable thermopower. It is about 60 times larger compared to that of the same kind of 3-dot interferometer operating in the linear regime [12, 20]. Moreover, thermoelectric efficiency at the maximum power of the heat engine is somewhat large and we obtain values as high as 80 percent of the Carnot efficiency in the present non-linear regime. Another aspect of the present study on this AB heat engine is that it can have great tunability either by changing magnetic flux, external gate voltage, or temperature bias. This will enable us to provide electrostatic-driven control of charge and heat current and its thermoelectric response under different relevant physical conditions achievable from the experimental point of view. It is well

known that two-dimensional electron gas superstructures based on metallic or GaAs/AlGaAs can be suitable candidates for the implementation of the Aharonov–Bohm quantum heat engine and they can produce devices with vigorous productivity over a wide range of system parameters [59]. Further experiments or simulations on this subject may instigate various theoretical work to address the effect of interactions and elastic or inelastic scattering effects that may bring on corrections due to an altered internal potential.

One natural question may arise: how the power-efficiency of our set-up may be modified in the presence of elastic or inelastic scattering? The (e-e) or electron-phonon interaction will affect the power-efficiency performance. With the help of our previous study [31], we have seen that only the even harmonic modes are present for the charge current in the presence of an elastic scattering process. More investigations are underway and will be published elsewhere. Our investigation establishes that one can trade-off the power-efficiency of an AB thermoelectric heat engine by tuning the setup's quantum coherence and harmonic modes. The fascinating relationship between power-efficiency, external magnetic flux, gate voltage, temperature bias, and harmonic modes make this Aharonov–Bohm loop a prototypical platform for the execution of a distinctive class of phase-tunable thermoelectric quantum machines operating at cryogenic temperatures in the highly nonlinear regime. It is also observed that the symmetric triple-dot setup provides more tunability to control the thermoelectric response compared to its asymmetric counterpart. Finally, in the context of quantum technologies, our studies on the coherent structure of AB interferometer provide a useful way to manipulate thermodynamic operational modes of quantum thermoelectric heat engines and such kind of setup might be at the core of several innovative thermoelectric quantum devices.

Appendix A: Equations of Motion

The model setup of the triple-quantum-dot AB interferometer has been discussed in Section II. We now solve this model and calculate the observables in the non-equilibrium steady-state. Since the model is noninteracting, we can use the Nonequilibrium Green's Function (NEGF) approach to calculate its steady-state characteristics [43, 44]. The NEGF technique has been widely used in the past years for investigating the transport properties in mesoscopic systems and molecular junctions [45]. We follow the equation of motion approach for the derivations [46]. In this method, we solve the Heisenberg equations of motion (EOM) for the bath variables and then substitute them back in the EOM for the subsystem (dots) variables. We obtain a quantum Langevin

equation (QLE) for the subsystem as follows:

$$\begin{aligned} \frac{d\hat{d}_i(t)}{dt} = & -i \left[\epsilon_i \hat{d}_i + \sum_{j \neq i} t_{ij} \hat{d}_j e^{i\phi_{ij}} \right] - i \sum_{\nu=S,D} \hat{\eta}_i^\nu(t) \\ & - i \sum_{j,\nu=S,D} \int_{t_0}^t \Sigma_{i,j}^{\nu,+}(t-t') \hat{d}_j(t') dt'. \end{aligned} \quad (\text{A1})$$

Here we use the indices $i = 1, 2, 3$ to identify the three dots. The terms $\hat{\eta}_i^S$ and $\hat{\eta}_i^D$ are referred to as the noise induced on the subsystem by the source and drain, respectively and they are expressed as

$$\begin{aligned} \hat{\eta}_i^S &= \sum_k V_{i,k}^S g_{Sk}^+(t-t_0) \hat{c}_{Sk}(t_0), \\ \hat{\eta}_i^D &= \sum_k V_{i,k}^D g_{Dk}^+(t-t_0) \hat{c}_{Dk}(t_0). \end{aligned} \quad (\text{A2})$$

The retarded Green's functions of the isolated reservoirs are given by

$$\begin{aligned} g_{Sk}^+(t) &= -ie^{-i\epsilon_{Sk}t} \theta(t), \\ g_{Dk}^+(t) &= -ie^{-i\epsilon_{Dk}t} \theta(t). \end{aligned} \quad (\text{A3})$$

For the initial condition, we take factorized states for the total density matrix $\rho_T(t_0) = \rho_S \otimes \rho_D \otimes \rho(t_0)$, with empty dots and reservoirs prepared in a grand canonical state

$$\hat{\rho}_\nu = \frac{e^{-(\hat{H}_\nu - \mu_\nu \hat{N})/T_\nu}}{\text{Tr}[e^{-(\hat{H}_\nu - \mu_\nu \hat{N})/T_\nu}]}, \quad (\text{A4})$$

where T_ν and μ_ν are the temperatures and chemical potentials of the Fermi sea with $\nu = S, D$. The state of the subsystem is denoted by the reduced density matrix ρ . Using the initial conditions we obtained the noise correlation as follows

$$\begin{aligned} \langle \hat{\eta}_i^{\dagger S}(t) \hat{\eta}_{i'}^S(\tau) \rangle &= \sum_k V_{i,k}^{S*} e^{i\omega_k(t-\tau)} V_{i',k}^S f_S(\omega_k), \\ \langle \hat{\eta}_i^{\dagger D}(t) \hat{\eta}_{i'}^D(\tau) \rangle &= \sum_k V_{i,k}^{D*} e^{i\omega_k(t-\tau)} V_{i',k}^D f_D(\omega_k), \end{aligned} \quad (\text{A5})$$

with the Fermi function $f_\nu = [e^{(\omega - \mu_\nu)/T_\nu} + 1]^{-1}$ for the reservoir $\nu = S, D$ with μ_ν and T_ν be the corresponding chemical potential and temperature, respectively. In the Heisenberg picture, the expectation value of an observable A can be obtained as $\langle \hat{A}(t) \rangle = \text{Tr}_T[\rho_T(t_0) \hat{A}(t)]$, tracing over all degrees of freedom. The steady-state properties are obtained by taking the limits $t_0 \rightarrow -\infty$ and $t \rightarrow \infty$. We can now take the Fourier transform of Eq. (A1) using the convolution theorem with the convention $\tilde{d}_i(\omega) = \int_{-\infty}^{\infty} dt d_i(t) e^{i\omega t}$ and $\tilde{\eta}_i^\nu(\omega) = \int_{-\infty}^{\infty} dt \eta_i^\nu(t) e^{i\omega t}$ and the result in matrix form is

$$\tilde{d}_i(\omega) = \sum_j G_{i,j}^+(\omega) [\tilde{\eta}_j^S(\omega) + \tilde{\eta}_j^D(\omega)]. \quad (\text{A6})$$

Here, the retarded Green's function is given by

$$G^\pm(\omega) = [\omega I - \hat{H}_{TQD} - \Sigma_S^\pm(\omega) - \Sigma_D^\pm(\omega)]^{-1}, \quad (\text{A7})$$

where I is a (3×3) identity matrix and the self-energies are defined as:

$$\begin{aligned}\Sigma_S^\pm(\omega) &= \sum_k V_{1,k}^S g_S^\pm(\omega) V_{1,k}^{S*}, \\ \Sigma_D^\pm(\omega) &= \sum_k V_{3,k}^D g_D^\pm(\omega) V_{1,k}^{D*}.\end{aligned}\quad (\text{A8})$$

Here, $g_S^\pm(\omega)$ and $g_D^\pm(\omega)$ are given by the Fourier transform of Eq. (A3). In the wide-band limit and when the density of states of the metallic lead is energy independent, the real part of the self-energy term vanishes. Then we can define the hybridization matrix from the relation $\Sigma^\pm = -i\Gamma/2$:

$$\Gamma_{i,i'}^\nu = 2\pi \sum_{k,\nu} V_{i',k}^{\nu*} V_{i,k}^\nu \delta(\omega - \omega_k). \quad (\text{A9})$$

We may take $V_{i,k}^\nu$ as real constants, independent of the level index and reservoir state, resulting in $\Gamma_{1,1}^S = \gamma_S$ and $\Gamma_{3,3}^D = \gamma_D$, where γ_ν (energy independent) describes the coupling between the dots and metallic leads. We consider degenerate dot energies $\epsilon_1 = \epsilon_2 = \epsilon_3 = \epsilon_d$ and set $t_{ij} = t$ to obtain the retarded Green's function.

Appendix B: Physical units

Our paper uses the natural unit convention $\hbar = c = e = k_B$ for simulation. At this point, it is useful to express our results in terms of physical units. Thermo-electric heat engine based on a quantum dot (QD) embedded into a semiconductor nanowire has been studied experimentally [60]. One can obtain physical units using the relation $\hbar\gamma = k_B T_a$, where γ is the dot-lead coupling and T_a is the average temperature. Considering $T_a = 1$ K, we obtain $\gamma = 1.31 \times 10^{11}$ Hz and based on this value of γ we convert all other parameters to physical units. In simulations, we use the dot-lead coupling strength, $\gamma = 0.05$ which translates into $\gamma = 6.5$ GHz. The parameters $t = \gamma$, $\epsilon_d = 8\gamma$, $T_S = 12\gamma$, $T_D = 2\gamma$, $\mu_D = -\mu_S = 4\gamma$ translate to $t = 4.3$ μ eV, $\epsilon_d = 34.4$ μ eV, $T_S = 0.6$ K, $T_D = 0.1$ K, and $\mu_D = -\mu_S = 17.2$ μ eV, respectively.

In physical units, the Landauer- Buttiker formula for electric current from the source (S) is defined by

$$I_S = \frac{e}{h} \int_{-\infty}^{\infty} d\omega [T_{SD}(\omega, \phi) f_S(\omega) - T_{DS}(\omega, \phi) f_D(\omega)]. \quad (\text{B1})$$

and the heat current from the source (S) is defined by

$$Q_S = \frac{1}{h} \int_{-\infty}^{\infty} d\omega (\omega - \mu_S) [T_{SD}(\omega, \phi) f_S(\omega) - T_{DS}(\omega, \phi) f_D(\omega)], \quad (\text{B2})$$

where f_ν , ($\nu = S, D$), is the Fermi distribution function, e is the charge of the electron and h is Planck's constant. Now, the output power generated is given by $P = (\Delta\mu/e)I_S$, where $\Delta\mu = \mu_D - \mu_S$. In physical units, $\omega = \mathcal{O}(\gamma = 1.31 \times 10^{11}$ Hz). To express the output power in physical units, the factor $\gamma = 1.31 \times 10^{11}$ Hz = 13.76×10^{-24} J should be multiplied with both $\Delta\mu$ and I_S . With this, we focus on Fig. 5 and express the output power in physical units for three different regimes i.e., (a) $t/\gamma < 1$, (b) $t/\gamma = 1$ and (c) $t/\gamma > 1$. Considering Fig. 5, for $t/\gamma < 1$ regime, we obtain the maximum output power, $P_{max} = 0.0024$ corresponding to an electric current from the source, $I_S = 0.0073$ which translates to $P_{max} \sim 0.7$ fW and $I_S = 0.024$ nA, respectively. Similarly, for $t/\gamma = 1$ regime, the maximum output power, $P_{max} = 0.0082$ corresponding to an electric current of $I_S = 0.026$ translates to $P_{max} \sim 2.35$ fW and $I_S = 0.086$ nA, respectively. For $t/\gamma > 1$ regime, maximum output power $P_{max} = 0.0071$ corresponds to electric current $I_S = 0.0262$ translates to $P_{max} \sim 2.04$ fW and $I_S = 0.087$ nA, respectively.

Now we consider Fig. 8(c) and obtain the maximum output power for different asymmetric dot-lead coupling ratios in physical units. We define the asymmetric parameter as $x = \gamma_S/\gamma_D$. For $x = 0.5$, we obtain a maximum output power $P_{max} = 0.0098 = 2.81$ fW. Similarly, for $x = 1$, $P_{max} = 0.0122 = 3.5$ fW; for $x = 1.5$, $P_{max} = 0.0125 = 3.58$ fW; for $x = 2$, $P_{max} = 0.0120 = 3.44$ fW; for $x = 2.5$, $P_{max} = 0.0114 = 3.27$ fW.

ACKNOWLEDGEMENTS

J.B. acknowledges the financial support received from IIT Bhubaneswar in the form of an Institute Research Fellowship. M.B. gratefully acknowledges financial support from the Department of Science and Technology (DST), India under the Core grant (Project No. CRG/2020//001768).

[1] G. Benenti, G. Casati, K. Saito, and R. S. Whitney, Fundamental aspects of steady-state conversion of heat to work at the nanoscale, *Physics Reports* **694**, 1 (2017).

[2] H. van Houten, L. W. Molenkamp, C. W. J. Beenakker, and C. T. Foxon, Thermo-electric properties of quantum point contacts, *Semiconductor Science and Technology* **7**, B215 (1992).

- [3] R. S. Whitney, Most efficient quantum thermoelectric at finite power output, *Phys. Rev. Lett.* **112**, 130601 (2014).
- [4] R. S. Whitney, Finding the quantum thermoelectric with maximal efficiency and minimal entropy production at given power output, *Phys. Rev. B* **91**, 115425 (2015).
- [5] R. S. Whitney, R. Sánchez, and J. Splettstoesser, Quantum thermodynamics of nanoscale thermoelectrics and electronic devices, in *Thermodynamics in the Quantum Regime: Fundamental Aspects and New Directions*, edited by F. Binder, L. A. Correa, C. Gogolin, J. Anders, and G. Adesso (Springer International Publishing, Cham, 2018) pp. 175–206.
- [6] N. Taniguchi, Quantum control of nonlinear thermoelectricity at the nanoscale, *Phys. Rev. B* **101**, 115404 (2020).
- [7] Y. M. Blanter, C. Bruder, R. Fazio, and H. Schoeller, Aharonov-Bohm-type oscillations of thermopower in a quantum-dot ring geometry, *Phys. Rev. B* **55**, 4069 (1997).
- [8] P. P. Hofer and B. Sothmann, Quantum heat engines based on electronic Mach-Zehnder interferometers, *Phys. Rev. B* **91**, 195406 (2015).
- [9] C. J. Lambert, H. Sadeghi, and Q. H. Al-Galiby, Quantum-interference-enhanced thermoelectricity in single molecules and molecular films, *Comptes Rendus Physique* **17**, 1084 (2016).
- [10] P. Samuelsson, S. Kheradsoud, and B. Sothmann, Optimal quantum interference thermoelectric heat engine with edge states, *Phys. Rev. Lett.* **118**, 256801 (2017).
- [11] S.-Y. Hwang, F. Giazotto, and B. Sothmann, Phase-coherent heat circulator based on multiterminal Josephson junctions, *Phys. Rev. Applied* **10**, 044062 (2018).
- [12] G. Haack and F. Giazotto, Efficient and tunable Aharonov-Bohm quantum heat engine, *Phys. Rev. B* **100**, 235442 (2019).
- [13] F. Giazotto, T. T. Heikkilä, A. Luukanen, A. M. Savin, and J. P. Pekola, Opportunities for mesoscopies in thermometry and refrigeration: Physics and applications, *Rev. Mod. Phys.* **78**, 217 (2006).
- [14] D. Sánchez and R. López, Nonlinear phenomena in quantum thermoelectrics and heat, *Comptes Rendus Physique* **17**, 1060 (2016).
- [15] Y. Aharonov and D. Bohm, Significance of electromagnetic potentials in the quantum theory, *Phys. Rev.* **115**, 485 (1959).
- [16] M. Büttiker, Y. Imry, and M. Y. Azbel, Quantum oscillations in one-dimensional normal-metal rings, *Phys. Rev. A* **30**, 1982 (1984).
- [17] A. L. Yeyati and M. Büttiker, Aharonov-Bohm oscillations in a mesoscopic ring with a quantum dot, *Phys. Rev. B* **52**, R14360 (1995).
- [18] O. Entin-Wohlman and A. Aharony, Three-terminal thermoelectric transport under broken time-reversal symmetry, *Phys. Rev. B* **85**, 085401 (2012).
- [19] J. Lu, Y. Liu, R. Wang, C. Wang, and J.-H. Jiang, Optimal efficiency and power, and their trade-off in three-terminal quantum thermoelectric engines with two output electric currents, *Phys. Rev. B* **100**, 115438 (2019).
- [20] G. Haack and F. Giazotto, Nonlinear regime for enhanced performance of an Aharonov-Bohm heat engine, *AVS Quantum Science* **3**, 046801 (2021).
- [21] S. Hershfield, K. A. Muttalib, and B. J. Nartowt, Nonlinear thermoelectric transport: A class of nanodevices for high efficiency and large power output, *Phys. Rev. B* **88**, 085426 (2013).
- [22] M. Dresselhaus, G. Chen, M. Tang, R. Yang, H. Lee, D. Wang, Z. Ren, J.-P. Fleurial, and P. Gogna, New directions for low-dimensional thermoelectric materials, *Advanced Materials* **19**, 1043 (2007).
- [23] T. E. Humphrey, R. Newbury, R. P. Taylor, and H. Linke, Reversible quantum Brownian heat engines for electrons, *Phys. Rev. Lett.* **89**, 116801 (2002).
- [24] A. A. Clerk, X. Waintal, and P. W. Brouwer, Fano resonances as a probe of phase coherence in quantum dots, *Phys. Rev. Lett.* **86**, 4636 (2001).
- [25] C. M. Finch, V. M. García-Suárez, and C. J. Lambert, Giant thermopower and figure of merit in single-molecule devices, *Phys. Rev. B* **79**, 033405 (2009).
- [26] G. Gómez-Silva, O. Ávalos Ovando, M. L. Ladrón de Guevara, and P. A. Orellana, Enhancement of thermoelectric efficiency and violation of the Wiedemann-Franz law due to Fano effect, *Journal of Applied Physics* **111**, 053704 (2012).
- [27] V. M. García-Suárez, R. Ferradás, and J. Ferrer, Impact of Fano and Breit-Wigner resonances in the thermoelectric properties of nanoscale junctions, *Phys. Rev. B* **88**, 235417 (2013).
- [28] G. Bevilacqua, G. Grosso, G. Menichetti, and G. Pastori Parravicini, Thermoelectric efficiency of nanoscale devices in the linear regime, *Phys. Rev. B* **94**, 245419 (2016).
- [29] G. Menichetti, G. Grosso, and G. P. Parravicini, Analytic treatment of the thermoelectric properties for two coupled quantum dots threaded by magnetic fields, *Journal of Physics Communications* **2**, 055026 (2018).
- [30] L. Cui, R. Miao, C. Jiang, E. Meyhofer, and P. Reddy, Perspective: Thermal and thermoelectric transport in molecular junctions, *The Journal of Chemical Physics* **146**, 092201 (2017).
- [31] M. Bandyopadhyay, S. Ghosh, A. Dubey, and S. Bedkihal, Flux dependent current rectification in geometrically symmetric interconnected triple-dot Aharonov-Bohm interferometer, *Physica E: Low-dimensional Systems and Nanostructures* **133**, 114786 (2021).
- [32] B. D’Anjou and W. A. Coish, Anomalous magnetotransport through reflection-symmetric artificial molecules, *Phys. Rev. B* **87**, 085443 (2013).
- [33] A. D. Stone and Y. Imry, Periodicity of the Aharonov-Bohm effect in normal-metal rings, *Phys. Rev. Lett.* **56**, 189 (1986).
- [34] A. Yacoby, R. Schuster, and M. Heiblum, Phase rigidity and $h/2e$ oscillations in a single-ring Aharonov-Bohm experiment, *Phys. Rev. B* **53**, 9583 (1996).
- [35] G. Hackenbroich and H. A. Weidenmüller, Transmission through a quantum dot in an Aharonov-Bohm ring, *Phys. Rev. Lett.* **76**, 110 (1996).
- [36] A. E. Hansen, A. Kristensen, S. Pedersen, C. B. Sørensen, and P. E. Lindelof, Mesoscopic decoherence in Aharonov-Bohm rings, *Phys. Rev. B* **64**, 045327 (2001).
- [37] B. Grbić, R. Leturcq, T. Ihn, K. Ensslin, D. Reuter, and A. D. Wieck, Aharonov-Bohm oscillations in p-type GaAs quantum rings, *Physica E: Low-dimensional Systems and Nanostructures* **40**, 1273 (2008).
- [38] L. Gaudreau, A. S. Sachrajda, S. Studenikin, A. Kam, F. Delgado, Y. P. Shim, M. Korkusinski, and P. Hawrylak, Coherent transport through a ring of three quantum dots, *Phys. Rev. B* **80**, 075415 (2009).

- [39] G.-Y. Yi, C. Jiang, L.-L. Zhang, S.-R. Zhong, H. Chu, and W.-J. Gong, Manipulability of the kondo effect in a t-shaped triple-quantum-dot structure, *Phys. Rev. B* **102**, 085418 (2020).
- [40] L.-L. Zhang and W.-J. Gong, Transport properties in a non-hermitian triple-quantum-dot structure, *Phys. Rev. A* **95**, 062123 (2017).
- [41] G.-Y. Yi, X.-Q. Wang, W.-J. Gong, H.-N. Wu, and X.-H. Chen, Josephson effect in a triple-quantum-dot ring with one dot coupled to superconductors: Numerical renormalization group calculations, *Physics Letters A* **380**, 1385 (2016).
- [42] G.-Y. Yi, X.-Q. Wang, H.-N. Wu, and W.-J. Gong, Nonlocal magnetic configuration controlling realized in a triple-quantum-dot josephson junction, *Physica E: Low-dimensional Systems and Nanostructures* **81**, 26 (2016).
- [43] Y. Meir and N. S. Wingreen, Landauer formula for the current through an interacting electron region, *Phys. Rev. Lett.* **68**, 2512 (1992).
- [44] J.-S. Wang, B. K. Agarwalla, H. Li, and J. Thingna, Nonequilibrium Green's function method for quantum thermal transport, *Front. Phys.* **9**, 673 (2014).
- [45] J. Fransson, *Non-Equilibrium Nano-Physics: A Many-Body Approach*, Vol. 809 (Springer, Dordrecht, 2010).
- [46] A. Dhar and D. Sen, Nonequilibrium Green's function formalism and the problem of bound states, *Phys. Rev. B* **73**, 085119 (2006).
- [47] S. Datta, *Electronic transport in mesoscopic systems* (Cambridge university press, 1997).
- [48] U. Sivan and Y. Imry, Multichannel landauer formula for thermoelectric transport with application to thermopower near the mobility edge, *Phys. Rev. B* **33**, 551 (1986).
- [49] P. N. Butcher, Thermal and electrical transport formalism for electronic microstructures with many terminals, *Journal of Physics: Condensed Matter* **2**, 4869 (1990).
- [50] F. Mazza, R. Bosisio, G. Benenti, V. Giovannetti, R. Fazio, and F. Taddei, Thermoelectric efficiency of three-terminal quantum thermal machines, *New Journal of Physics* **16**, 085001 (2014).
- [51] S. Carnot, Reflections on the motive power of fire, and on machines fitted to develop that power, Paris: Bachelier **108**, 1824 (1824).
- [52] C. Emary, Dark states in the magnetotransport through triple quantum dots, *Phys. Rev. B* **76**, 245319 (2007).
- [53] F. Delgado, Y.-P. Shim, M. Korkusinski, and P. Hawrylak, Theory of spin, electronic, and transport properties of the lateral triple quantum dot molecule in a magnetic field, *Phys. Rev. B* **76**, 115332 (2007).
- [54] F. Delgado and P. Hawrylak, Theory of electronic transport through a triple quantum dot in the presence of magnetic field, *Journal of Physics: Condensed Matter* **20**, 315207 (2008).
- [55] C. Pörtl, C. Emary, and T. Brandes, Two-particle dark state in the transport through a triple quantum dot, *Phys. Rev. B* **80**, 115313 (2009).
- [56] I. Weymann, B. R. Bulka, and J. Barnaś, Dark states in transport through triple quantum dots: The role of cotunneling, *Phys. Rev. B* **83**, 195302 (2011).
- [57] F. Domínguez, S. Kohler, and G. Platero, Phonon-mediated decoherence in triple quantum dot interferometers, *Phys. Rev. B* **83**, 235319 (2011).
- [58] J. P. Carini, K. A. Muttalib, and S. R. Nagel, Origin of the Bohm-Aharonov effect with half flux quanta, *Phys. Rev. Lett.* **53**, 102 (1984).
- [59] M. C. Rogge and R. J. Haug, Two-path transport measurements on a triple quantum dot, *Phys. Rev. B* **77**, 193306 (2008).
- [60] M. Josefsson, A. Svilans, A. M. Burke, E. A. Hoffmann, S. Fahlvik, C. Thelander, M. Leijnse, and H. Linke, A quantum-dot heat engine operating close to the thermodynamic efficiency limits, *Nature Nanotech* **13**, 920–924 (2018).